Elucidating Energy Pathways through Simultaneous Measurement of Absorption and Transmission in a Coupled Plasmonic-Photonic Cavity

Feng Pan, [†] Kevin C. Smith, [‖] Hoang L. Nguyen, [†] Kassandra A. Knapper, [†] David J. Masiello, [§*] and Randall H. Goldsmith[†*]

[†]Department of Chemistry, University of Wisconsin-Madison, Madison, WI 53706-1322, USA

[‖]Department of Physics, University of Washington, Seattle, Washington, 98195-1560, USA

[§]Department of Chemistry, University of Washington, Seattle, Washington, 98195-1700, USA

Abstract

Control of light-matter interactions is central to numerous advances in quantum communication, information, and sensing. The relative ease in which interactions can be tailored in coupled plasmonic-photonic systems makes them ideal candidates for investigation. To exert control over the interaction between photons and plasmons, it is essential to identify the underlying energy pathways which influence the system's dynamics and determine the critical system parameters, such as the coupling strength and dissipation rates. However, in coupled systems which dissipate energy through multiple competing pathways, simultaneously resolving all parameters from a single experiment is challenging as typical observables such as absorption and scattering each probe only a particular path. In this work, we simultaneously measure both photothermal absorption and two-sided optical transmission in a coupled plasmonic-photonic resonator consisting of plasmonic gold nanorods deposited on a toroidal whispering-gallery-mode optical microresonator. We then present an analytical model which predicts and explains the distinct line shapes observed and quantifies the contribution of each system parameter. By combining this model with experiment, we extract all system parameters with a dynamic range spanning nine orders of magnitude. Our combined approach provides a full description of plasmonic-photonic energy dynamics in a weakly coupled optical system, a necessary step for future applications that rely on tunability of dissipation and coupling.

Keywords

Whispering Gallery Mode, Plasmonic Cavity, Photonic Cavity, Purcell Enhancement, Single-Particle Spectroscopy

In 1946 Purcell theoretically demonstrated that the spontaneous emission rate of an emitter can be enhanced by its dielectric environment,[1] prompting the birth of what is now known as cavity quantum electrodynamics (cQED). Following this discovery and its subsequent experimental confirmation,[2] cQED has remained an active area of both theoretical and experimental research and has found application in a variety of fields such as quantum communication and information,[3-10] sensing,[11-14] and cavity-controlled chemistry.[15-22] The development of cQED is intertwined with developments in nanoscience and nanofabrication. In particular, recent years have seen a boom in cQED experiments due to the emergence of sophisticated techniques for fabrication of high-quality-factor, chip-scale optical microcavities[23] and deterministic positioning of "artificial atoms" such as quantum dots and plasmonic nanoparticles on optical microcavities.[24-28]

Whispering-gallery-mode (WGM) microcavities are especially attractive due to the attainable ultrahigh quality factor (up to 10^8)[23, 29] of their optical modes which can allow for Purcell factors as large as 190.[30] In recent work, it has been predicted that this factor may be improved even further by coupling the cavity modes to the localized surface plasmon (LSP) of a metal nanoparticle, effectively creating a hybrid plasmonic-photonic resonator which inherits the ultrasmall mode volume of the LSP while retaining the large quality factor of the WGMs.[31-37] In order to both understand and leverage the light-matter interactions in such a system, it is imperative to accurately determine the multiple intrinsic damping rates, the LSP-WGM coupling strength, and additional extrinsic dissipation rates introduced through the measurement. However, these quantities can span many orders of magnitude, particularly in weakly coupled systems, making it difficult for a single experiment to capture all of the information.

Many methods have been used to probe light-matter interactions in cavity-matter systems, including far-field detection of emitted or reflected photons,[25, 38-45] measurement of

transmitted/reflected photons in a waveguide coupled to the system,[24, 46-49] and single-particle absorption measurements.[31, 50] Specifically, photoluminescence or scattering measurements collect radiated energy in the far field, transmission/reflection measurements using a waveguide detects energy transferred from the WGM to the tapered fiber, and absorption measurements probe nonradiative dissipation. While these techniques are individually capable of revealing spectral signatures of the underlying light-matter interaction, each serves as a readout for only a particular dissipative pathway and cannot simultaneously resolve all parameters that govern energy flow within the system. For example, nonradiative and radiative damping rates can be inferred from absorption and scattering spectra, respectively, while a fiber-based one-sided transmission experiment inherently depends upon the rate of energy exchange between an optically pumped waveguide and the cavity to which it is coupled. Crucially, the linewidth of any spectral feature contains information about the total dissipation rate of the system but does not distinguish between the various dissipative pathways regardless of the observable. Thus, simultaneous measurement of multiple spectroscopic observables is needed for one to understand how energy is both distributed and dissipated via multiple pathways in a coupled cavity-matter system.

In this work we demonstrate the ability to simultaneously measure both photothermal absorption and optical transmission in a coupled plasmonic-photonic cavity consisting of plasmonic gold nanorods (AuNRs) deposited on a silica toroidal WGM microresonator.[23] Specifically, the transmission is measured in a two-sided[51] manner, where energy is input through a free-space pump laser and output through a fiber to which the LSP-WGM system is coupled. In contrast to previous studies on single AuNRs or quantum dots which have relied on measurements of scattering or photoluminescence, we measure photothermal absorption and two-sided transmission using a single photonic waveguide, where an individual AuNR is optically pumped

by a frequency-tunable free-space laser. AuNRs of a high aspect ratio (10:1) are used so that the longitudinal dipolar LSP is efficiently excited by our tunable, narrow-linewidth near-infrared free-space pump laser. Taken together, absorption and transmission encode sufficient information about

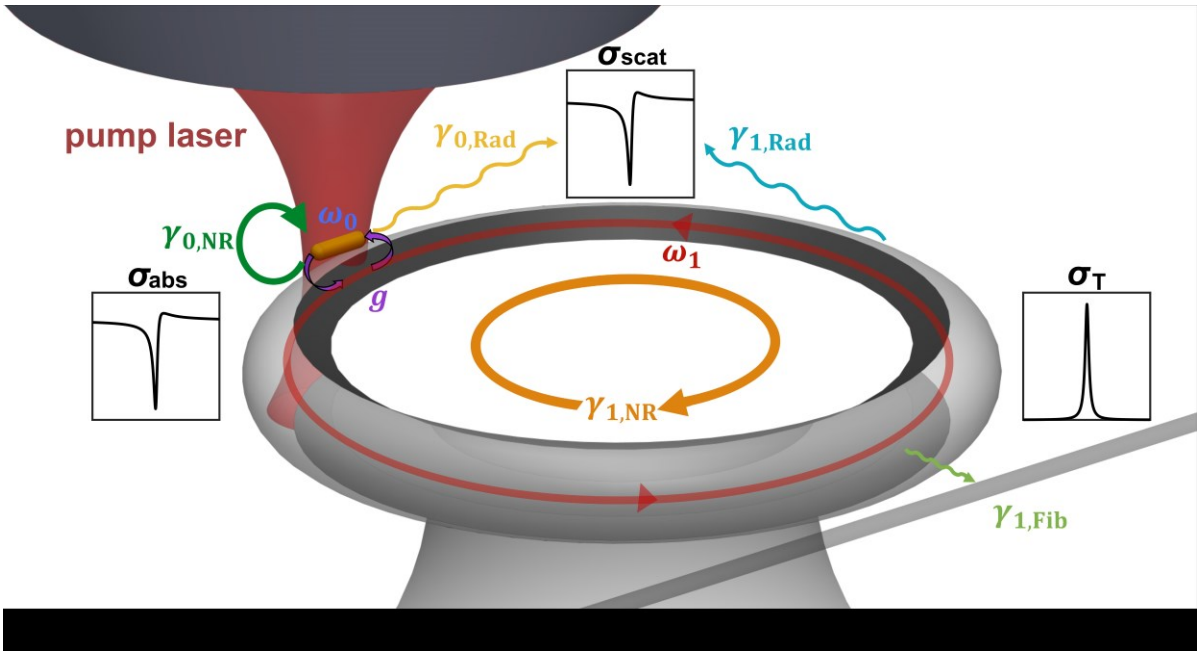

Figure 1. Schematic of dissipative coupled AuNR-microresonator system with all parameters (ω_0, $\gamma_{0,NR}$, $\gamma_{0,Rad}$, g, ω_1, $\gamma_{1,NR}$, $\gamma_{1,Rad}$, $\gamma_{1,Fib}$) as well as experimental observables (inset spectra). Energy enters the coupled system via pump laser excitation of the dipolar LSP of the AuNR and is dissipated through various pathways. Once excited, the LSP decays through both radiative ($\gamma_{0,Rad}$) and nonradiative ($\gamma_{0,NR}$) means, and in addition may exchange energy with the microresonator via LSP-WGM coupling (g). The WGM likewise may exchange energy with the LSP or decay via outcoupling to the waveguide ($\gamma_{1,Fib}$) in addition to radiative ($\gamma_{1,Rad}$) and nonradiative ($\gamma_{1,NR}$) dissipation channels. The conservation of energy through these various pathways in the steady state is reflected by the equality between the extinction cross-section (σ_{ext}), which is a measure of the rate at which energy enters the system, and the sum of the absorption (σ_{abs}), scattering (σ_{scat}) and transmission (σ_T) cross-sections (inset equation), each of which probes a particular dissipative pathway.

the individual damping rates and mutual coupling strength of the LSP and WGM such that all relevant system parameters (see Figure 1) may be determined. Figure 1 illustrates these system parameters as well as the complete set of observables that both determine and are defined by their specific values.

Absorption and Two-Sided Transmission

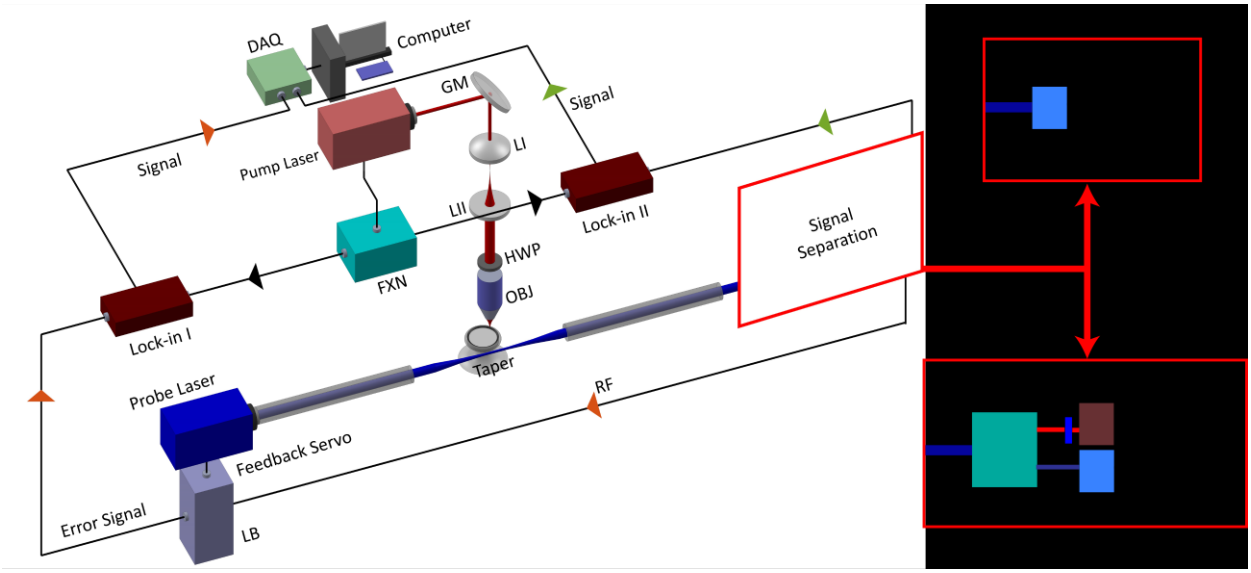

Figure 2. Experimental setup for simultaneous measurement of absorption and two-sided transmission. LI: lens I, LII: lens II, GM: galvo mirrors, FXN: function generator, Lock-in: lock-in amplifier, HWP: half-wave plate, OBJ: objective, LB: lock box, WDM: wavelength division multiplexer, SP: short-pass optical filter, PDA: adjustable-gain photodiode detector, APD: avalanche photodiode detector, DAQ: National Instruments LabView data acquisition card, RF: radio-frequency electrical signal generated from APD, DC: kHz to DC electrical signal generated from APD. The red box indicates where either an electrical separation (top) or optical separation (bottom) is implemented. Arrows of different colors represent photothermal absorption (orange) and transmission (green) measurements or references (black).

As described previously[31, 50, 52], photothermal absorption spectroscopy is performed with separate pump and probe beams. As shown in the experimental scheme of Figure 2, a narrow-band tunable probe laser coupled to a tapered optical fiber interrogates the microresonator WGMs via evanescent coupling. At the other end of the optical fiber is an avalanche photodiode (APD) to allow monitoring of probe beam transmission. The probe beam is phase-modulated at radio frequencies (RF) and locked to the WGM resonance via the Pound-Drever-Hall locking scheme.[50] Simultaneously, a pump beam is focused to a near diffraction-limited spot and overlapped with individual nanoparticles on the microresonator surface. The pump beam is amplitude-modulated at kHz frequencies to maximize the signal-to-noise ratio. This double modulation scheme is

capable of resolving resonance shifts down to under one attometer.[50] The amount of resonance shift is then used to compute the power absorbed by the AuNRs with the aid of a FDTD (COMSOL) simulation of the steady-state temperature increase within the microresonator.[50] The pump laser is raster-scanned over the microresonator to search for single AuNRs sparsely deposited on the resonator. Once located, an absorption spectrum is obtained by wavelength-scanning the tunable continuous-wave pump laser polarized along the long axis of the AuNR. High-resolution photothermal absorption spectra show distinctive sharp Fano antiresonance line shapes (shown schematically as σ_{abs} in Figure 1), indicative of mutual interaction between photonic and plasmonic modes.[31, 50, 53]

Concurrent with photothermal absorption, we now measure the two-sided transmission (σ_T in Figure 1), i.e., the power transmitted from the free-space pump laser through the plasmonic-photonic system and into the same tapered fiber used for the above photothermal measurement. In order to implement the simultaneous measurement of photothermal absorption and two-sided transmission, we first relied on the use of an electrical signal diplexer in an electrical separation scheme that can discriminate RF signal from much slower oscillatory signal (kHz to DC, hereafter called DC), as shown in Figure 2. Both signals are generated by the APD detector. As above, the photothermal absorption signal is decoded from pump-induced phase shifts in the RF signal through both the local oscillator used for phase-modulation of the probe beam and a lock-in amplifier. At the same time, the DC signal is directly connected to a second lock-in amplifier for measurement of the kHz-modulated two-sided transmission. This strategy relies on the fact that while the photothermal and two-sided transmission signals are both modulated via the pump beam's (kHz) modulation, only the photothermal signal is additionally modulated at RF frequencies. However, high-resolution spectra collected over several spectral ranges show that

signal measured through the DC channel (Figure 3a, middle) closely follows the asymmetric Fano line shapes measured through the RF channel (Figure 3a, top). In addition, low-resolution spectra measured through the two channels both show broad spectral signatures of the LSP (see Figure S2). The similar spectral line shapes in absorption and transmission (Figure 3a, top and middle) can be understood by examining the resonance shift induced by photothermal response of the microresonator, shown in Figure 3b. The DC channel measures the amplitude difference (labeled with $\mathbf{T_{Electrical}}$) in the vertical direction which is proportional to the WGM resonance shift (labeled with **A**) in the horizontal direction due to photothermal effect, and therefore, the DC signal provides a scaled replica of the photothermal absorption spectrum. Thus, this scheme, cannot discriminate the two-sided transmission from the photothermal signal.

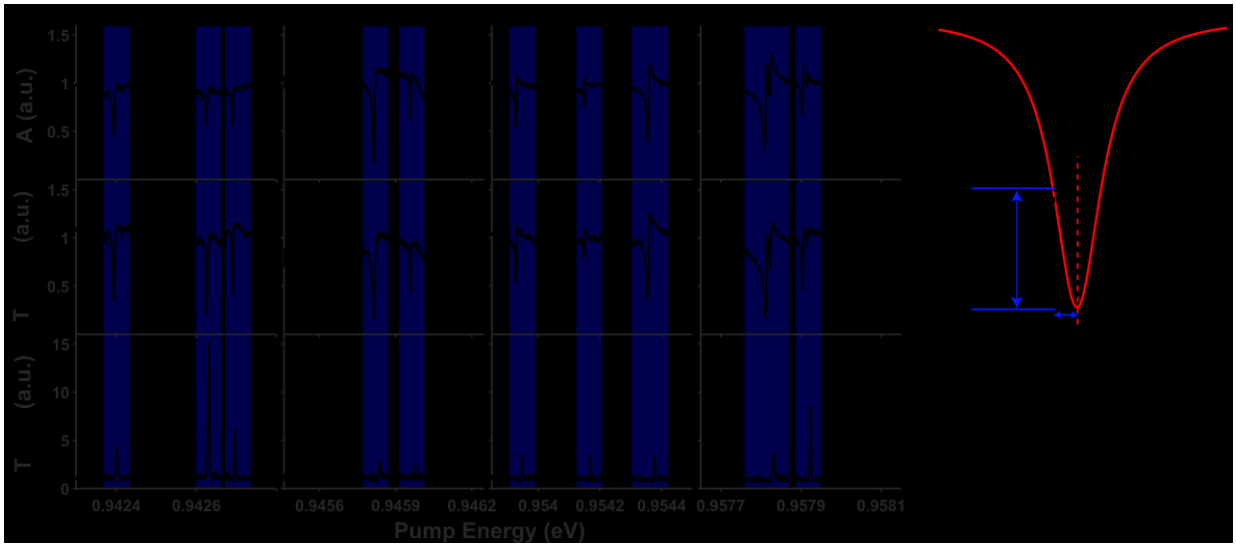

Figure 3. Simultaneous spectral measurements. (a) photothermal absorption (**A**) measured through the RF channel from APD (top); transmission ($\mathbf{T_{Electrical}}$) measured through DC channel from APD (middle); transmission ($\mathbf{T_{Optical}}$) measured with the WDM included and detected via the PDA (bottom). Note that the resonance "teeth" of transmission ($\mathbf{T_{Optical}}$) are not exactly lined up with other two observables. In this case, $\mathbf{T_{Electrical}}$ and **A** were measured simultaneously, but $\mathbf{T_{Optical}}$ was measured later and the laser scanning actuator experienced minor motion hysteresis. (b) Schematic illustration of how photothermal and transmission measurements are conveyed through RF and DC channels when the pump laser induces a resonance shift.

In comparison, the simple optical separation scheme shown in Figure 2 enables the distinction between photons transmitted through the coupled plasmonic-photonic cavity system from the pump beam (λ = 1275-1355 nm) and those photons originating in the probe beam (λ = 1550-1570 nm) and employed for photothermal spectroscopy. A combination of a wavelength division multiplexer (WDM), short-pass optical filter, and second photodetector (PDA) then allows for a simultaneous direct measurement of photons of different wavelengths traveling through the taper, revealing dramatically distinct spectral features, as shown in the bottom row of Figure 3a. At each WGM energy position lies a resonant line shape that is conspicuously different from the Fano antiresonance seen in the absorption spectra. Measurements on different AuNRs and microresonators show these same phenomena (see Figure S1). High-resolution spectra over a full spectral range taken through the two channels also show distinct spectral features where the

spectrally broad LSP resonance measured via photothermal absorption is replaced by a series of resonance "teeth" in the two-sided transmission spectra (see Figure S3). These distinct spectral behaviors are also robust over a range of pump laser modulation frequencies (Figure S4). The two-sided transmission signal is highly dependent on taper position relative to the microresonator, with certain positions rendering some WGMs inaccessible while other modes are viable channels for outcoupling photons to the taper (see Figures S8 and S12), as expected.[54] Taken together, adding a WDM-filtered detection channel enables one to realize the simultaneous measurement of absorption and two-sided transmission for a coupled LSP-WGM system using a single optical waveguide.

Modeling

The spectral features exposed by simultaneous absorption and transmission measurements can be well-understood through mathematical modeling of the various energy pathways available to the coupled LSP-WGM system. To that effect, we develop a coupled oscillator model which includes physically independent system parameters relevant to each dissipative process and, as will be shown, each spectral observable. While this model is derived from first principles (SI), simplifications informed by experimental results are made. For example, the distinct line shapes in transmission spectra indicate that the tapered fiber does not simply play a passive role in the interrogation of the coupled LSP-WGM system. Instead, the propagating modes of the tapered fiber are coupled to the WGMs of the microresonator through the mutual overlap of their evanescent fields. Because this coupling is weak, it manifests itself in the LSP-WGM dynamics as a taper-induced loss mechanism and the dynamics of the fiber modes need not be explicitly considered. In addition, quantum fluctuations, while typically included in input-output theory as a manifestation of the fluctuation-dissipation theorem,[51] are ignored here as all excitations are in the

many-quanta limit where classical effects dominate. Lastly, only a single WGM need be considered since the modes of the toroid are mutually orthogonal and therefore do not interact directly. Taking all of these considerations into account, the equations of motion for the LSP-WGM system may be written as

$$\begin{aligned} m\ddot{x} + m\gamma_{0,\mathrm{NR}}\dot{x} + m\omega_0^2 x + g\sqrt{\frac{m}{V}}\dot{q} &= \frac{2e^2}{3c^3}\dddot{x} + eE_{\mathrm{ext}}e^{-i\omega t} \\ \frac{1}{V}\ddot{q} + \frac{1}{V}\left(\gamma_{1,\mathrm{NR}} + \gamma_{1,\mathrm{Rad}} + \gamma_{1,\mathrm{Fib}}\right)\dot{q} + \frac{1}{V}\omega_1^2 q - g\sqrt{\frac{m}{V}}\dot{x} &= 0 \end{aligned} \tag{1}$$

where x and m are the oscillator amplitude and effective mass of the dipolar LSP along the AuNR's long axis, c is the speed of light, $E_{\mathrm{ext}}e^{-i\omega t}$ is the field of the pump laser incident on the AuNR, and the radiation reaction force (proportional to $\dddot{x}$ and e is the elementary charge) acting on the LSP has been included.[55] Where appropriate, the subscripts 0 and 1 are used to signify LSP and WGM parameters, respectively. On the second line, V is the mode volume of the WGM and q is related to its associated electric field by

$$\vec{E}(\vec{x}, t) = -\frac{\sqrt{4\pi}}{V}\dot{q}(t)\vec{f}(\vec{x}), \tag{2}$$

where the mode function[56, 57] $\vec{f}(\vec{x})$ is a solution to a generalized form of the vector Helmholtz equation appropriate for an isolated WGM resonator. Finally, appearing in both equations of motion is a term proportional to the coupling strength, g, determined (up to scaling factors) by the projection of the WGM mode function onto the long axis of the AuNR at its center, $\vec{r}_0$,

$$g = e\sqrt{\frac{4\pi}{mV}}\vec{f}(\vec{r}_0)\cdot\hat{x}. \tag{3}$$

While the equations of motion (Eq. 1) are similar to those used in our previous work[31, 50], here we explicitly differentiate between the various physical processes which contribute to the decay of both the LSP and WGM excitations. Each distinct damping rate is labeled by γ with a subscript denoting the relevant dissipative pathway. The LSP dissipates energy via nonradiative absorption ($\gamma_{0,\mathrm{NR}}$) and radiation into the far field ($\gamma_{0,\mathrm{Rad}} = 2e^2\omega^2/3mc^3$), while the WGM can decay through energy transfer to the fiber ($\gamma_{1,\mathrm{Fib}}$) in addition to dissipative processes intrinsic to the WGM, including material absorption, bending loss, and surface inhomogeneity scattering. According to the model, $\gamma_{1,\mathrm{Fib}}$ depends upon the mutual overlap of evanescent fields of WGMs and fiber taper modes. Additionally, energy may be transferred from the WGM to LSPs of undriven AuNRs on the surface of the toroid which in turn can absorb and radiate. While these taper-independent WGM decay pathways are each the result of physically distinct processes, all terminate in either heating the microresonator or liberating energy into the far-field via radiation, and therefore can be aggregated into a total nonradiative ($\gamma_{1,\mathrm{NR}}$) and radiative ($\gamma_{1,\mathrm{Rad}}$) damping rate.

Each dissipative pathway is associated with a distinct experimental observable; absorption measurements probe nonradiative dissipation, scattering measurements collect radiated energy in the far field, and the previously described two-sided transmission measurement detects energy transferred from the WGM to the tapered fiber. Accordingly, expressions for various cross-sections may be derived by computing the power dissipated in the steady state by the corresponding damping force in Eq. (1) and normalizing to the intensity of the pump laser incident on the AuNR (SI). Carrying out this procedure leads to the following expressions for the reduced absorption, scattering, and extinction (i.e., total) cross-sections

$$\frac{\sigma_{\text{abs}}}{\sigma_{\text{abs}}^{0}} = \frac{\tilde{\gamma}_{0,\text{NR}}}{\gamma_{0,\text{NR}}} F(\omega) \qquad \frac{\sigma_{\text{scat}}}{\sigma_{\text{scat}}^{0}} = \frac{\tilde{\gamma}_{0,\text{Rad}}}{\gamma_{0,\text{Rad}}} F(\omega) \qquad \frac{\sigma_{\text{ext}}}{\sigma_{\text{ext}}^{0}} = \frac{\tilde{\gamma}_{0,\text{Tot}}}{\gamma_{0,\text{Tot}}} F(\omega) \tag{4}$$

where the superscript 0 denotes the cross-section of the isolated LSP and

$$\tilde{\gamma}_{0,j}(\omega) = \gamma_{0,j} + \frac{\omega^2 g^2}{(\omega^2 - \omega_1^2)^2 + \omega^2 \gamma_{1,\text{Tot}}^2} \gamma_{1,j} \tag{5}$$

is the WGM-dressed LSP damping rate where j indicates a particular decay pathway (nonradiative, radiative, or total). Each reduced cross-section scales with the function

$$F(\omega) = \left| \frac{q_{\text{F}} + \epsilon}{\epsilon + i} \right|^2 \tag{6}$$

which depends on the scaled and shifted pump frequency $\epsilon(\omega) = (\omega^2 - \Omega^2)/\omega\Gamma$ where explicit forms for $\Omega(\omega)$ and $\Gamma(\omega)$ are given in the SI. In the limit where LSP damping dominates the coupled LSP-WGM dynamics $\left(\text{i.e.}, \gamma_{0,\text{Tot}} \gg \gamma_{1,\text{Tot}}, g\right)$, the complex-valued function $q_{\text{F}}(\omega) = (\Omega^2 - \omega_1^2 + i\omega\gamma_{1,\text{Tot}})/\omega\Gamma$ becomes approximately constant over the spectral width of the WGM and can thus be identified as a complex generalization of the Fano asymmetry parameter,[31] while $F(\omega)$ becomes the familiar Fano line shape[50, 53, 58] describing an antiresonant effect at pump frequencies near the WGM resonant frequency.

Because the two-sided transmission measurement is unique to the LSP-WGM system and not of the LSP itself, it is not sensible to normalize the transmission cross-section to that of the bare LSP. Instead, it can be shown (SI) that it takes the form,

$$\sigma_{\text{T}} = \frac{\gamma_{1,\text{Fib}}}{\gamma_{1,\text{Tot}}} \left(1 - \frac{\gamma_{0,\text{Tot}}}{\tilde{\gamma}_{0,\text{Tot}}}\right) \sigma_{\text{ext}}. \tag{7}$$

This expression, while different in form from the other cross-sections previously discussed, can be intuitively understood by considering the pathway taken by the transmitted energy prior to its detection in the tapered fiber: the extinction cross-section σ_{ext} characterizes the total fraction of energy imparted into the LSP by the incident pump laser per unit time in the steady state, while the two preceding factors (from right-to-left) describe the fraction of that energy that is transferred to the WGM and, finally, the fraction that is dissipated into the tapered fiber.

Analysis

While the above model alone yields a qualitative understanding of the physics underlying the coupled LSP-WGM system and the observables which probe its dissipative pathways, quantitative estimates of the parameters relevant to those observables may be obtained through a combination of theory and experimental data through least-squares fitting. Such a quantitative characterization of the system is compelling for a variety of reasons. An order-of-magnitude comparison between various parameters elucidates the breadth of timescales which play a role in the system dynamics, while an analysis of the coupling strength in relation to the dominant dissipative rates reveals where the system lies in the range of weak-to-strong coupling (our system is clearly in the weak coupling regime). In addition, an accurate parameter estimation is important for optimizing hybrid cavity design to control light-matter interactions, such as for maximum Purcell enhancement.[31]

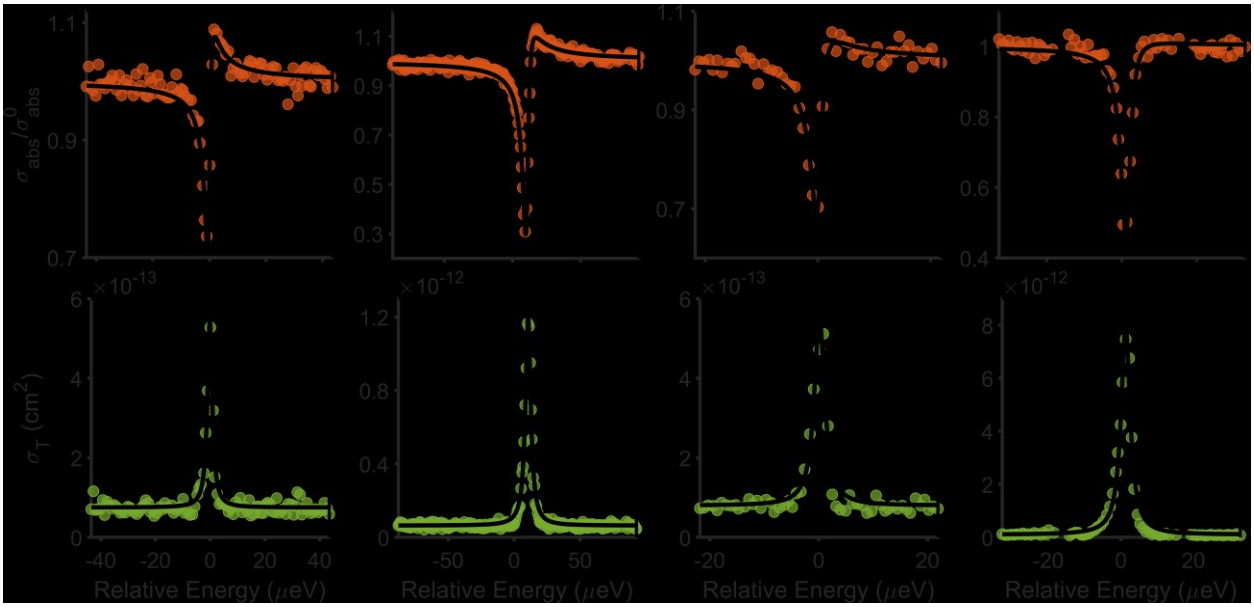

Figure 4. Simultaneous fits to reduced absorption cross-section (top) and transmission cross-section (bottom). Though relative energies are plotted here, absolute energies are used for further analysis.

Due to the multiple order-of-magnitude mismatch between LSP and WGM linewidths, both low- and high-resolution absorption spectral measurements are taken into consideration. The low-resolution scan characterizes the spectrally broad Lorentzian "envelope" of the LSP, while the high-resolution scan reveals spectrally narrow Fano line shapes in absorption[31, 50, 53, 58] and sharp resonance "teeth" in transmission, as discussed above. Parameter estimates are obtained through a two-step fitting procedure. First, LSP parameters (ω_0, $\gamma_{0,\mathrm{NR}}$, $\gamma_{0,\mathrm{Rad}}$) are extracted by fitting low-resolution absorption spectra to the bare LSP absorption cross-section

$$\sigma_{\mathrm{abs}}^{0}(\omega) = \frac{4\pi\omega^2}{c}\frac{\gamma_{0,\mathrm{NR}}}{(\omega^2-\omega_0^2)^2+\omega^2\gamma_{0,\mathrm{Tot}}^2}. \tag{8}$$

Subsequently, remaining parameters (ω_1, $\gamma_{1,\mathrm{NR}}$, $\gamma_{1,\mathrm{Rad}}$, $\gamma_{1,\mathrm{Fib}}$, g), are obtained through simultaneous fitting of high-resolution absorption and two-sided transmission spectra to Eqs. (4) and (7) with LSP parameters bound within 95% confidence intervals. Notably, all fits are carried

out on absolute measurements without artificial scaling parameters. Simultaneous fits over several spectral ranges that contain a large number of WGM resonances all show an excellent agreement between experimental measurements and the model, a few of which are shown in Figure 4 and Figure S7.

The plasmon natural frequency (ω_0) and nonradiative damping rate ($\gamma_{0,\mathrm{NR}}$) obtained from fits vary minimally between different WGM resonances, as shown in Figure 5a. The stepwise trend of ω_1 results from the fact that individual, well-separated spectral windows are surveyed, each containing multiple WGM resonances. Likewise, a similar stepwise trend is observed for the frequency-dependent LSP radiative damping rate $\gamma_{0,\mathrm{Rad}}(\omega)$ which here is evaluated at $\omega = \omega_1$. Analyzed WGMs consist of those at resonant frequencies both higher and lower than the frequency of the LSP (ω_0). Cavity intrinsic ($\gamma_{1,\mathrm{NR}}$ and $\gamma_{1,\mathrm{Rad}}$) and taper-induced ($\gamma_{1,\mathrm{Fib}}$) loss rates are less than those contributed by the LSP by over three orders of magnitude. We calculate the global mean of individual damping rates obtained from the fitting for each parameter. As shown in Table 1, fits to simultaneous absorption and transmission measurements make it possible to extract a high dynamic range of damping rates spread over six orders of magnitude. The LSP damping rates are comparable to those reported by Refs[45, 59, 60] reported for single AuNRs, while WGM damping rates are in accordance with typical Q factors (~10^6) of higher-order modes measured in toroidal microresonators with AuNRs deposited on the surface. As expected, the coupled LSP-WGM system is well within the weak coupling regime as the interaction energy g is multiple orders-of-magnitude smaller than the system's total damping rates ($\hbar g \sim 10^{-4}$ eV, $\hbar\gamma_{0,\mathrm{Tot}} \sim 10^{-2}$ eV, $\hbar\gamma_{1,\mathrm{Tot}} \sim 10^{-6}$ eV). $\gamma_{1,\mathrm{Fib}}$ is the smallest among WGM loss rates, suggesting the taper is under-coupled and can act as a weakly perturbative readout to examine those WGMs that interact with the LSP.

As seen by examining the standard deviation of the mean, the variation amongst LSP parameters is minimal in comparison to the WGM parameters. This is expected as all measurements were carried out for a single LSP with a well-defined resonance frequency and linewidth. In contrast, the mean and standard deviation of the mean for the WGM parameters compiles results across 12 distinct WGM resonances and variation is therefore expected. In particular, the fiber-induced loss rate $\gamma_{1,\mathrm{Fib}}$ and the coupling strength g depend crucially on the field profile of the particular WGM in question and therefore the standard deviation of the mean conveys important information about the range of attainable values for these parameters. Among all parameters, the most uncertain is the WGM radiative loss rate $\gamma_{1,\mathrm{Rad}}$. This is expected as we do not measure scattering and therefore do not directly probe the energy dissipated through radiative means. In other words, the absorption and two-sided transmission measurements provide sufficient information to extract the individual rates $\gamma_{1,\mathrm{NR}}$ and $\gamma_{1,\mathrm{Fib}}$, respectively, while the line shape in either observable may be used to determine the total linewidth $\gamma_{1,\mathrm{Tot}}$. The radiative rate $\gamma_{1,\mathrm{Rad}}$ is inferred through a combination of these independent measurements along with the relation $\gamma_{1,\mathrm{Rad}} = \gamma_{1,\mathrm{Tot}} - \gamma_{1,\mathrm{NR}} - \gamma_{1,\mathrm{Fib}}$. A more direct determination of $\gamma_{1,\mathrm{Rad}}$ would be possible through a scattering measurement simultaneous with the absorption and transmission measurements.

In order to evaluate the sensitivity of each observable on the coupling strength and the various damping rates, we compute all derived observables using the global mean of all fit parameters and examine the effect of the parameters' variation upon that observable (SI), as shown in Figure 5b. The LSP damping rates, particularly $\gamma_{0,\mathrm{NR}}$, dominate the contribution to σ_{abs}, σ_{scat}, and σ_{ext}. However, σ_{T} is more sensitive to the variations of WGM damping rates and coupling strength. Overall, through simultaneous measurement of absorption and transmission, we are able to fully describe this weakly coupled system even though its parameter space spans nearly nine

orders of magnitude in energy. This capability provides a foundation for deterministic control and design of specific dissipative channels for specific purposes.

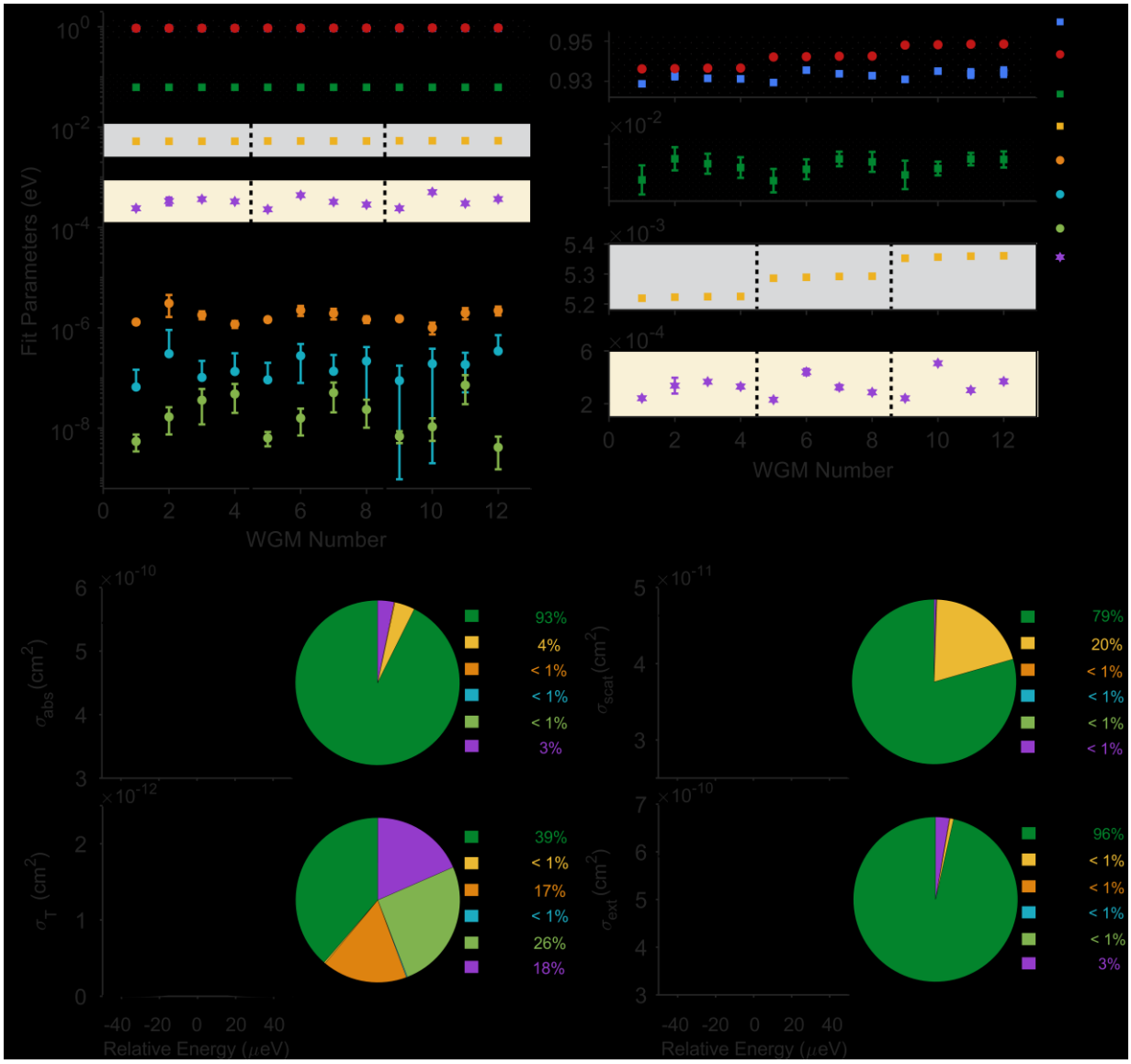

Figure 5. (a) All fit parameters in log scale (left side) obtained from simultaneous fits to experimental data in well-separated spectral windows indicated by dark dashed lines. Scaling these parameters between frequency and energy units is accomplished by an implicit factor of $\hbar$. Zoom-in plots in linear scale (right side) for better clarity. The arrow on the second panel indicates a range of $5 \times 10^{-6}\ eV$. (b) Computed spectra (left side) based on the global mean of all fit parameters and pie charts (right side) for the parameters' contributions to the corresponding cross-sections.

One example of an application would be to tailor far-field radiation by controlling the influence of the photonic environment on a single nanorod's polarizability. A similar scheme was used in an array of nanorods coupled to a single WGM through backaction.[43] With the addition of a far-field scattering measurement and theoretical modeling, a complete accounting of every

photon entering and exiting the system would be possible. As dictated by energy conservation, the sum of the powers scattered, absorbed, and transmitted must equal the laser power extinguished when averaged over an optical cycle. This conservation is made explicit through the sum rule obeyed by the observables in Eqs. (4) and (7),

$$\sigma_{\text{ext}}(\omega) = \sigma_{\text{abs}}(\omega) + \sigma_{\text{scat}}(\omega) + \sigma_{\text{T}}(\omega), \tag{9}$$

which can be derived by appealing to Newton's equations (SI). Nevertheless, even without a scattering measurement, it is possible to extract parameter values from absorption and transmission measurements and subsequently extrapolate the system's scattering behavior from the model. This method of determining system parameters can be combined with previously reported methods for tuning the plasmonic resonance based on thermal annealing[31] to exert unprecedented control over plasmonic-photonic mode mixing and energy flow.

Table 1. The mean and standard deviation of the mean for all fit parameters.

	$\hbar\omega_0$ (eV)	$\hbar\omega_1$ (eV)	$\hbar\gamma_{0,\text{NR}}$ (meV)	$\hbar\gamma_{0,\text{Rad}}$ (meV)	$\hbar g$ (meV)	$\hbar\gamma_{1,\text{NR}}$ (μeV)	$\hbar\gamma_{1,\text{Rad}}$ (μeV)	$\hbar\gamma_{1,\text{Fib}}$ (neV)
Mean	0.9326	0.9426	62.20249	5.293	0.332	1.74	0.18	26
S.D.	0.0001	0.0002	0.00009	0.002	0.004	0.04	0.02	1

In general, the emergent properties of cavity-matter systems are determined by the dissipation rates and couplings such as those quantitatively determined in this work. The balance of these parameters must often be precisely controlled in order to achieve certain functionality across a breadth of applications. For example, tunability of LSP and WGM resonance energies in a coupled plasmonic-photonic cavity is crucial for maximizing Purcell enhancement.[31] A perfect balance of gain and loss is imperative for creation of exceptional points in parity-time symmetric

systems.[13, 61] To achieve strong cavity-matter coupling, a significant disparity between coupling and total loss is necessary.[62, 63] The ability to dial-in specific coupling strengths and resonance energies is a critical requirement for creation of nonlinear coupled cavities arrays for quantum simulation,[64-66] quantum error correction,[67] and optical signal processing.[68] Creation of routing systems in photonic circuits requires precise control of photon transfer rates between component cavities.[69] Realization of all these applications depends upon convenient experimental techniques, such as those presented here, to determine intrinsic system parameters across many timescales.

In summary, using a single tapered optical fiber, we demonstrate the simultaneous measurement of photothermal absorption and two-sided transmission from individual plasmonic nanorods coupled to an optical microresonator. These observables allow us to track down the distribution and dissipation of energy through multiple competing pathways. We also present a model of the coupled plasmonic-photonic system that we use to fit the measured data and extract the damping parameters as well as the LSP-WGM coupling strength with a high dynamic range spanning up to nine orders of magnitude, fully describing the LSP-WGM dynamics in a weakly coupled system. These combined experimental and theoretical techniques may be useful for future spectroscopic investigation of weakly or strongly coupled plasmonic, excitonic, and photonic systems with dissipation and coupling spanning a wide range of timescales. This quantitative understanding is necessary to leverage light-matter interactions through manipulating specific dissipation channels and/or coupling for applications in quantum communication and quantum information science,[3-9] single-molecule detection,[70, 71] and cavity-controlled chemistry.[15-22]

Methods

Sample preparation

Toroidal microresonators were fabricated as described previously.[72] A vortexed stock solution of gold nanorods (25×256 nm^2, Nanopartz A12-25-1400) was diluted by 200 times in Millipore water. Prior to deposition onto resonators, the diluted solution was vortexed again. The solution was then drop-cast onto a chip of resonators and allowed to settle for 5 minutes before spinning for 1 minute at 3000 rpm.

Spectroscopic measurement

The previously described apparatus[31, 50, 52] is modified for simultaneous measurement of photothermal and two-sided transmission signal. A tunable laser (Newport TLB-6728) is used as the probe laser. Unless otherwise stated, a wavelength division multiplexer (Thorlabs, WD1350A, 1310 nm/1550 nm) is used to split two colors of photons (~1310 nm and ~1550 nm) co-propagating in a single-mode fiber (SMF-28e+, Corning). The photons of two different colors are then measured by two photodetectors (PDA10CS, APD430C), respectively. A free-space pump beam (~1310 nm) from another tunable laser (Thorlabs TLK-L1300) is delivered through a high numerical aperture (NA) air objective (Nikon, 60X, NA 0.95). The pump beam is amplitude-modulated at kHz and results in heat dissipation from AuNR to the microresonator, which shifts WGM resonance. The photothermal signal is then de-modulated by a lock-in amplifier (Ametek, Signal Recovery 7265). The amount of resonance shift is related to the actual power absorbed by AuNR using COMSOL simulation and AuNR's photoluminescence quantum yield (assumed to be zero[73]). In contrast to photothermal measurement, the two-sided transmission photons (~1310 nm) are collected through the other port of WDM and passed through an optical filter (Edmund Optics, 1450 nm, 25 mm, OD 2 Short-pass filter) for blocking photons at ~1550 nm. The filtered transmitted photons are measured by the PDA photodetector. The transmission signal is then de-modulated by a second lock-in amplifier. The two lock-in amplifiers are synchronized and

externally connected with a refence square wave at kHz from the same function generator. More details in SI.

Supporting Information

Information on (1) experimental details, including (i) experimental setup, (ii) data acquisition methods and (iii) investigation of pump laser modulation's effect on spectra. Also (2) modeling LSP-WGM interaction and derivation of cross-sections and other expressions. Also (3) data analysis, including (i) fitting details and extra simultaneous fits, (ii) examination of some WGM damping parameters' dependence on taper relative position, (iii) method for evaluating contribution of LSP and WGM parameters to each observable, and (iv) characterization of angular structure of WGMs via transmission measurement.

Corresponding Authors

* E-mail: rhg@chem.wisc.edu; masiello@chem.washington.edu.

Funding

We acknowledge support from the National Science Foundation under awards CHE-1836482 (R.H.G.), CHE-1836506 (D.J.M), DMR-1610345 (R.H.G.) and CHE-1664684 (D.J.M.).

Author Contributions

FP acquired data with help from HLN and RHG. KCS performed modeling and calculations with help from DJM. KCS and FP analyzed data with help from RHG and DJM. KAK fabricated the resonators. FP and KCS wrote the manuscript together with help from all co-authors. FP and KCS contributed equally to this work.

Notes

The authors declare no competing financial interests.

References

1. Purcell, E. M. *Phys. Rev.* **1946,** 69.

2. Goy, P.; Raimond, J. M.; Gross, M.; Haroche, S. *Phys. Rev. Lett.* **1983,** 50, 1903-1906.

3. Li, Y.-H.; Zhou, Z.-Y.; Xu, Z.-H.; Xu, L.-X.; Shi, B.-S.; Guo, G.-C. *Phys. Rev. A* **2016,** 94, 043810.

4. De Greve, K.; Yu, L.; McMahon, P. L.; Pelc, J. S.; Natarajan, C. M.; Kim, N. Y.; Abe, E.; Maier, S.; Schneider, C.; Kamp, M.; Höfling, S.; Hadfield, R. H.; Forchel, A.; Fejer, M. M.; Yamamoto, Y. *Nature* **2012,** 491, 421-425.

5. Imamoğlu, A.; Awschalom, D. D.; Burkard, G.; DiVincenzo, D. P.; Loss, D.; Sherwin, M.; Small, A. *Phys. Rev. Lett.* **1999,** 83, 4204-4207.

6. Pellizzari, T.; Gardiner, S. A.; Cirac, J. I.; Zoller, P. *Phys. Rev. Lett.* **1995,** 75, 3788-3791.

7. Zheng, S.-B.; Guo, G.-C. *Phys. Rev. Lett.* **2000,** 85, 2392-2395.

8. Kimble, H. J. *Nature* **2008,** 453, 1023-1030.

9. Sillanpää, M. A.; Park, J. I.; Simmonds, R. W. *Nature* **2007,** 449, 438-442.

10. Wang, D.; Kelkar, H.; Martin-Cano, D.; Rattenbacher, D.; Shkarin, A.; Utikal, T.; Götzinger, S.; Sandoghdar, V. *Nat. Phys.* **2019,** 15, 483-489.

11. McKeever, J.; Buck, J. R.; Boozer, A. D.; Kimble, H. J. *Phys. Rev. Lett.* **2004,** 93, 143601.

12. Münstermann, P.; Fischer, T.; Maunz, P.; Pinkse, P. W. H.; Rempe, G. *Phys. Rev. Lett.* **1999,** 82, 3791-3794.

13. Peng, B.; Özdemir, Ş. K.; Lei, F.; Monifi, F.; Gianfreda, M.; Long, G. L.; Fan, S.; Nori, F.; Bender, C. M.; Yang, L. *Nat. Phys.* **2014,** 10, 394.

14. Özdemir, Ş. K.; Rotter, S.; Nori, F.; Yang, L. *Nat. Mater.* **2019,** 18, 783-798.

15. Herrera, F.; Spano, F. C. *Phys. Rev. Lett.* **2016,** 116, 238301.

16. Schäfer, C.; Ruggenthaler, M.; Appel, H.; Rubio, A. *Proc. Natl. Acad. Sci. U. S. A.* **2019,** 116, 4883-4892.

17. Dunkelberger, A. D.; Spann, B. T.; Fears, K. P.; Simpkins, B. S.; Owrutsky, J. C. *Nat. Commun.* **2016,** 7, 13504.

18. Zhong, X.; Chervy, T.; Zhang, L.; Thomas, A.; George, J.; Genet, C.; Hutchison, J. A.; Ebbesen, T. W. *Angew. Chem. Int. Ed.* **2017,** 56, 9034-9038.

19. Du, M.; Ribeiro, R. F.; Yuen-Zhou, J. *Chem* **2019,** 5, 1167-1181.

20. Lather, J.; Bhatt, P.; Thomas, A.; Ebbesen, T. W.; George, J. *Angew. Chem. Int. Ed.* **2019,** 58, 1-5.

21. Thomas, A.; George, J.; Shalabney, A.; Dryzhakov, M.; Varma, S. J.; Moran, J.; Chervy, T.; Zhong, X.; Devaux, E.; Genet, C.; Hutchison, J. A.; Ebbesen, T. W. *Angew. Chem. Int. Ed.* **2016,** 55, 11462-11466.

22. Thomas, A.; Lethuillier-Karl, L.; Nagarajan, K.; Vergauwe, R. M. A.; George, J.; Chervy, T.; Shalabney, A.; Devaux, E.; Genet, C.; Moran, J.; Ebbesen, T. W. *Science* **2019,** 363, 615-619.

23. Vahala, K. J. *Nature* **2003,** 424, 839-846.

24. Srinivasan, K.; Painter, O. *Nature* **2007,** 450, 862-865.

25. Ohta, R.; Ota, Y.; Nomura, M.; Kumagai, N.; Ishida, S.; Iwamoto, S.; Arakawa, Y. *Appl. Phys. Lett.* **2011,** 98, 173104.

26. Lodahl, P.; Mahmoodian, S.; Stobbe, S. *Rev. Mod. Phys.* **2015,** 87, 347-400.

27. Hennessy, K.; Badolato, A.; Winger, M.; Gerace, D.; Atatüre, M.; Gulde, S.; Fält, S.; Hu, E. L.; Imamoğlu, A. *Nature* **2007,** 445, 896-899.

28. Chen, Y.; Ryou, A.; Friedfeld, M. R.; Fryett, T.; Whitehead, J.; Cossairt, B. M.; Majumdar, A. *Nano Lett.* **2018,** 18, 6404-6410.

29. Armani, D. K.; Kippenberg, T. J.; Spillane, S. M.; Vahala, K. J. *Nature* **2003,** 421, 925-928.

30. Gayral, B.; Gérard, J. M.; Lemaître, A.; Dupuis, C.; Manin, L.; Pelouard, J. L. *Appl. Phys. Lett.* **1999,** 75, 1908-1910.

31. Thakkar, N.; Rea, M. T.; Smith, K. C.; Heylman, K. D.; Quillin, S. C.; Knapper, K. A.; Horak, E. H.; Masiello, D. J.; Goldsmith, R. H. *Nano Lett.* **2017,** 17, 6927-6934.

32. Doeleman, H. M.; Verhagen, E.; Koenderink, A. F. *ACS Photonics* **2016,** 3, 1943-1951.

33. Shopova, S. I.; Rajmangal, R.; Holler, S.; Arnold, S. *Appl. Phys. Lett.* **2011,** 98, 243104.

34. Santiago-Cordoba, M. A.; Boriskina, S. V.; Vollmer, F.; Demirel, M. C. *Appl. Phys. Lett.* **2011,** 99, 073701.

35. Boriskina, S. V.; Reinhard, B. M. *Proc. Natl. Acad. Sci. U. S. A.* **2011,** 108, 3147-3151.

36. Shopova, S. I.; Blackledge, C. W.; Rosenberger, A. T. *Appl. Phys. B* **2008,** 93, 183-187.

37. Ahn, W.; Boriskina, S. V.; Hong, Y.; Reinhard, B. M. *ACS Nano* **2012,** 6, 951-960.

38. Badolato, A.; Hennessy, K.; Atatüre, M.; Dreiser, J.; Hu, E.; Petroff, P. M.; Imamoğlu, A. *Science* **2005,** 308, 1158-1161.

39. Englund, D.; Fattal, D.; Waks, E.; Solomon, G.; Zhang, B.; Nakaoka, T.; Arakawa, Y.; Yamamoto, Y.; Vučković, J. *Phys. Rev. Lett.* **2005,** 95, 013904.

40. Englund, D.; Faraon, A.; Fushman, I.; Stoltz, N.; Petroff, P.; Vučković, J. *Nature* **2007,** 450, 857-861.

41. Liu, J.-N.; Huang, Q.; Liu, K.-K.; Singamaneni, S.; Cunningham, B. T. *Nano Lett.* **2017,** 17, 7569-7577.

42. Solomon, G. S.; Pelton, M.; Yamamoto, Y. *Phys. Rev. Lett.* **2001,** 86, 3903-3906.

43. Ruesink, F.; Doeleman, H. M.; Verhagen, E.; Koenderink, A. F. *Phys. Rev. Lett.* **2018,** 120, 206101.

44. Wang, P.; Wang, Y.; Yang, Z.; Guo, X.; Lin, X.; Yu, X.-C.; Xiao, Y.-F.; Fang, W.; Zhang, L.; Lu, G.; Gong, Q.; Tong, L. *Nano Lett.* **2015,** 15, 7581-7586.

45. Sönnichsen, C.; Franzl, T.; Wilk, T.; von Plessen, G.; Feldmann, J.; Wilson, O.; Mulvaney, P. *Phys. Rev. Lett.* **2002,** 88, 077402.

46. Ruesink, F.; Doeleman, H. M.; Hendrikx, R.; Koenderink, A. F.; Verhagen, E. *Phys. Rev. Lett.* **2015,** 115, 203904.

47. Peng, P.; Liu, Y.-C.; Xu, D.; Cao, Q.-T.; Lu, G.; Gong, Q.; Xiao, Y.-F. *Phys. Rev. Lett.* **2017,** 119, 233901.

48. Srinivasan, K.; Painter, O.; Stintz, A.; Krishna, S. *Appl. Phys. Lett.* **2007,** 91, 091102.

49. Xiao, Y.-F.; Liu, Y.-C.; Li, B.-B.; Chen, Y.-L.; Li, Y.; Gong, Q. *Phys. Rev. A* **2012,** 85, 031805.

50. Heylman, K. D.; Thakkar, N.; Horak, E. H.; Quillin, S. C.; Cherqui, C.; Knapper, K. A.; Masiello, D. J.; Goldsmith, R. H. *Nat. Photonics* **2016,** 10, 788-795.

51. Gardiner, C. W.; Collett, M. J. *Phys. Rev. A* **1985,** 31, 3761-3774.

52. Horak, E. H.; Rea, M. T.; Heylman, K. D.; Gelbwaser-Klimovsky, D.; Saikin, S. K.; Thompson, B. J.; Kohler, D. D.; Knapper, K. A.; Wei, W.; Pan, F.; Gopalan, P.; Wright, J. C.; Aspuru-Guzik, A.; Goldsmith, R. H. *Nano Lett.* **2018,** 18, 1600-1607.

53. Fano, U. *Phys. Rev.* **1961,** 124, 1866-1878.

54. Lin, G.; Qian, B.; Oručević, F.; Candela, Y.; Jager, J. B.; Cai, Z.; Lefèvre-Seguin, V.; Hare, J. *Opt. Lett.* **2010,** 35, 583-585.

55. Jackson, J. D., *Classical Electrodynamics (3rd ed.)*. John Wiley & Sons: New York, 1999.

56. Vernooy, D. W.; Furusawa, A.; Georgiades, N. P.; Ilchenko, V. S.; Kimble, H. J. *Phys. Rev. A* **1998,** 57, R2293-R2296.

57. Dalton, B. J.; Guerra, E. S.; Knight, P. L. *Phys. Rev. A* **1996,** 54, 2292-2313.

58. Miroshnichenko, A. E.; Flach, S.; Kivshar, Y. S. *Rev. Mod. Phys.* **2010,** 82, 2257-2298.

59. Juvé, V.; Cardinal, M. F.; Lombardi, A.; Crut, A.; Maioli, P.; Pérez-Juste, J.; Liz-Marzán, L. M.; Del Fatti, N.; Vallée, F. *Nano Lett.* **2013,** 13, 2234-2240.

60. Li, Z.; Mao, W.; Devadas, M. S.; Hartland, G. V. *Nano Lett.* **2015,** 15, 7731-7735.

61. Bender, C. M.; Boettcher, S. *Phys. Rev. Lett.* **1998,** 80, 5243-5246.

62. Sanvitto, D.; Kéna-Cohen, S. *Nat. Mater.* **2016,** 15, 1061-1073.

63. Du, M.; Martínez-Martínez, L. A.; Ribeiro, R. F.; Hu, Z.; Menon, V. M.; Yuen-Zhou, J. *Chem. Sci.* **2018,** 9, 6659-6669.

64. Greentree, A. D.; Tahan, C.; Cole, J. H.; Hollenberg, L. C. L. *Nat. Phys.* **2006,** 2, 856-861.

65. Carusotto, I.; Ciuti, C. *Rev. Mod. Phys.* **2013,** 85, 299-366.

66. Majumdar, A.; Rundquist, A.; Bajcsy, M.; Dasika, V. D.; Bank, S. R.; Vučković, J. *Phys. Rev. B* **2012,** 86, 195312.

67. Kerckhoff, J.; Nurdin, H. I.; Pavlichin, D. S.; Mabuchi, H. *Phys. Rev. Lett.* **2010,** 105, 040502.

68. Mabuchi, H. *Appl. Phys. Lett.* **2011,** 99, 153103.

69. Almeida, V. R.; Barrios, C. A.; Panepucci, R. R.; Lipson, M. *Nature* **2004,** 431, 1081-1084.

70. Baaske, M. D.; Foreman, M. R.; Vollmer, F. *Nat. Nanotech.* **2014,** 9, 933-939.

71. Dantham, V. R.; Holler, S.; Barbre, C.; Keng, D.; Kolchenko, V.; Arnold, S. *Nano Lett.* **2013,** 13, 3347-3351.

72. Heylman, K. D.; Goldsmith, R. H. *Appl. Phys. Lett.* **2013,** 103, 211116.

73. Link, S.; El-Sayed, M. A. *J. Phys. Chem. B* **1999,** 103, 8410-8426.